RSC Advances

PAPER

View Article Online
View Journal | View Issue

Cite this: *RSC Adv.*, 2017, **7**, 55034

Peculiar electronic, strong in-plane and out-of-plane second harmonic generation and piezoelectric properties of atom-thick α-M_2X_3 (M = Ga, In; X = S, Se): role of spontaneous electric dipole orientations†

Lei Hu* and Xuri Huang*

Second harmonic generation (SHG) and piezoelectric properties of two-dimensional (2D) materials are sparking great interest. However, out-of-plane SHG in 2D materials has been rarely reported; the theoretical out-of-plane piezoelectric response in atom-thick 2D materials is very limited at the present stage. α-M_2X_3 monolayers exhibit out-of-plane spontaneous polarizations, promising out-of-plane SHG and piezoelectricity. Here, we perform first-principles calculations of the electronic, SHG and piezoelectric properties of single- and few-layer α-M_2X_3. Results indicate the bandgaps of α-M_2X_3 monolayers are in the visible range, and become much narrower as the layer number goes up. Furthermore, the narrower bandgaps are broadened by more than 1.00 eV by switching the electric dipole orientation in few-layer α-M_2X_3. α-M_2X_3 monolayers exhibit superior in-plane and out-of-plane SHG properties; in particular, their out-of-plane SHG coefficients are comparable with those of GaAs crystals. Furthermore, the out-of-plane SHG coefficients can be effectively tuned by switching the electric dipole orientation in α-M_2X_3 few-layers. α-M_2X_3 monolayers exhibit superior in-plane and considerable out-of-plane piezoelectricity, and the latter is significantly enhanced in bilayer α-M_2X_3 because of the built-in electric field originating from the parallel electric dipoles. Our work will stimulate research on the ultrathin 2D photo detection, SHG and piezoelectric devices.

Received 6th October 2017
Accepted 27th November 2017

DOI: 10.1039/c7ra11014f

rsc.li/rsc-advances

1. Introduction

Second harmonic generation (SHG) and piezoelectric properties caused by noncentrosymmetry in two-dimensional (2D) atom-thick materials are sparking great interest. For instance, 2D MoS_2,[1,2] GaSe,[3,4] SiC,[5] BN[6] and GeC[7] nanosheets display fascinating prospects in ultrathin SHG devices. However, these 2D materials only exhibit in-plane SHG properties as they embody out-of-plane centrosymmetric characters, *i.e.* out-of-plane SHG has not been discovered in these 2D materials. On the other hand, monolayer BN,[8] MoS_2,[9] GaSe,[10] GaSSe,[11] buckled hexagonal compounds[12] and doped graphene,[13] have a wide range of applications including in mechanical stress sensors, actuators and energy harvesting devices[14] since they are piezoelectric. Even though a recent calculation has found strong out-of-plane piezoelectricity in multilayer MoSTe[15] and a recent experiment has shown that out-of-plane piezoelectricity occurs in multilayer (10 nm-thick) α-In_2Se_3 flakes,[16] the obtained out-of-plane piezoelectricity in atom-thick 2D materials such as monolayers[11–13] and bilayers is very limited. This makes it impossible to fabricate effective ultrathin 2D piezoelectric devices allowing out-of-plane mechanical–electrical energy conversions.

On the other hand, 2D nanosheets exfoliated from α- and β-In_2Se_3 bulk crystals are attracting great attention in the aspects of the thermal conductivity, phase transformation,[17,18] photoresponsibility,[19,20] sensitivity,[21] dielectric[22] and optical properties.[23] The electric field perpendicular to α- and β-In_2Se_3 monolayers induce a semiconductor to metal transition.[24] Remarkably, the class of α-M_2X_3 ferroelectric monolayers exhibit in-plane and out-of-plane reversible spontaneous polarizations,[25] promising in-plane and out-of-plane SHG and piezoelectric responses. Indeed, out-of-plane SHG has been recently discovered in monolayer α-In_2Se_3; however the features and magnitude of the SHG coefficients are still unknown.[16] Moreover, monolayer multiferroics exhibit very small out-of-plane SHG coefficients $\chi^{(2)}_{zzy}$ and $\chi^{(2)}_{zyz}$.[26] This simulates us to explore the SHG and piezoelectricity of α-M_2X_3 monolayers using first-principles calculations, expecting to find strong out-of-plane SHG and piezoelectricity.

Experiments indicate that the physical properties of In_2Se_3 multilayer nanosheets, such as optical bandgap[23] and thermal

Institute of Theoretical Chemistry, Jilin University, Changchun 130000, People's Republic of China. E-mail: 598450225@qq.com; Xurihuang12@gmail.com

† Electronic supplementary information (ESI) available. See DOI: 10.1039/c7ra11014f

conductivity,[17] show a strong layer-dependent behavior. These remind us to study the correlation between the layer thickness and the electronic, piezoelectric and SHG properties of atomic-thick M_2X_3 nanosheets. It should be noted that the nanosheet in our theoretical calculations is much thinner than that in previous experiments.[17,23] Moreover, the van der Waals heterostructure of α-In_2Se_3/WSe_2 shows a significant bandgap reduction when switching the electric dipole orientation of the In_2Se_3 layer. In essence, switching the electric orientation is changing stacking sequences. It has been shown SHG of few-layer GaSe nanosheets[27] and piezoelectricity of multilayer MoSTe[15] can be effectively tuned by using various stacking sequences. Therefore, it is meaningful to explore how the electric dipole orientation affects the electronic, piezoelectric and SHG properties of few-layer M_2X_3.

2. Calculation models and details

Single- and few-layer β-M_2X_3 nanosheets are centrosymmetric, their piezoelectricity and SHG vanish. We thereby study the electronic, piezoelectric and SHG properties of monolayer α-M_2X_3 (M = Ga, In; X = S, Se), and their top and side views are displayed in Fig. 1. To study the layer-dependent behavior, the bilayer and trilayer exfoliated from α-Ga_2S_3 and α-In_2Se_3 bulk crystals are considered, which are respectively named as AA and AAA stacking. Furthermore, to investigate the effect of the electric dipole orientation, bilayer AB is achieved by switching the electric dipole orientation of the bottom layer in AA, while trilayer ABA is attained by switching the electric dipole orientation of the middle layer in AAA.

All calculations are on the basis of the density functional theory (DFT) using the projector-augmented wave (PAW)[28] method as implemented in the Vienna *Ab initio* Simulation Package (VASP).[29–32] The generalized gradient approximation (GGA) parameterized by Perdew, Burke, and Ernzerhof (PBE)[33] with van der Waals (vdW) correction proposed by Crimme (DFT-D2)[34] is employed. The single electron wave functions are expanded with a large wave cutoff energy of 500 eV. To minimize the periodic interaction along the z axis, the vacuum spacing between adjacent nanosheets is set to be at least 20 Å. A gamma-centered k-point grid of $11 \times 11 \times 1$ is used to optimize geometry structures, and the convergence criteria for electronic and ionic relaxations are respectively set as 10^{-7} and 10^{-3} eV Å^{-1}. A k-point grid of $31 \times 31 \times 1$ is used to calculate piezoelectric coefficients of monolayers and few-layers. The more dense k-point grid of $60 \times 60 \times 1$ is used to obtain SHG coefficients of monolayers, while the k-point of $45 \times 45 \times 1$ is applied for few-layers.

3. Results and discussions

3.1. Structural properties

As shown in Fig. 1, α-M_2X_3 monolayers are five atoms thick, with atoms arranged in the sequence of X–M–X–M–X in the direction perpendicular to the layers. Table 1 summarizes the calculated in-plane constant a and effective thickness h of α-M_2X_3 monolayers. As the α-M_2X_3 bulk crystal contains three basic layers, the theoretical h of α-M_2X_3 monolayers is simply taken as 1/3 of the lattice constant c of optimized bulk crystals. The calculated h are larger than that of monolayer MX_2 (M = Mo, W; X = S, Se)[35] and GaX (X = S, Se, Te),[27] indicating a stronger SHG intensity in α-M_2X_3 monolayers than that in MoX_2 and GaX monolayers as the SHG intensity shows a quadratic dependence on the thickness, according to the dipole theory.[4] It is very convenient to identify layer numbers of α-M_2X_3 nanosheets using the effective thickness value in further experiments, which will accelerate explorations of their properties.

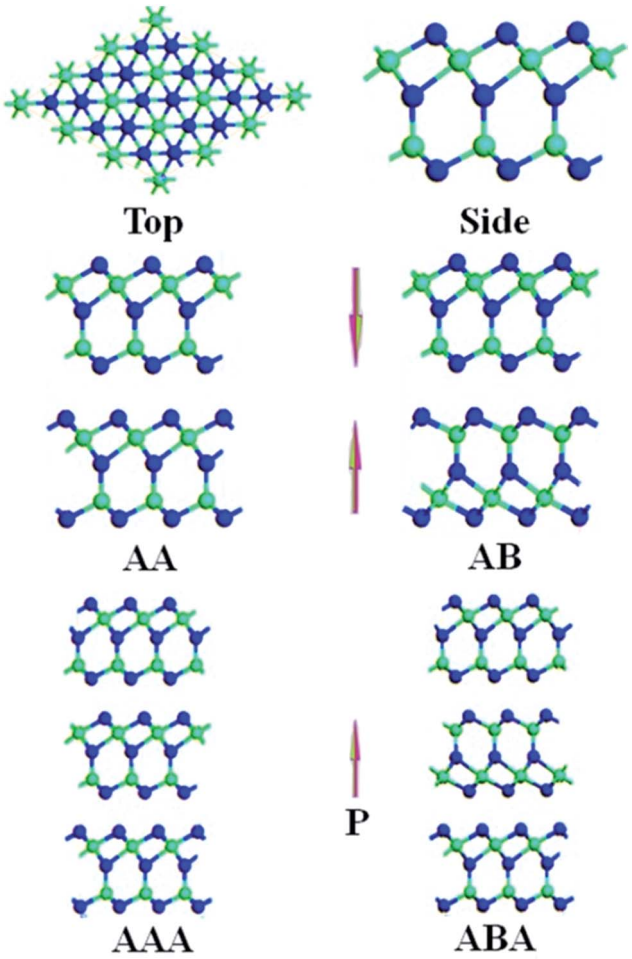

Fig. 1 Schematics of top and side views of monolayer α-M_2X_3. The green atoms denote M (M = Ga, In) atoms, while the blue atoms denote X (X = S, Se) atoms. This figure represents bilayer AB is achieved by switching the electric dipole orientation of the bottom α-M_2X_3 layer in bilayer AA, and trilayer ABA is obtained by switching the electric dipole orientation of the middle α-M_2X_3 layer in trilayer AAA.

Similar to previous calculations,[36] the formation energies of single- and few-layer α-M_2X_3 nanosheets are defined as $E_f = E/N - E_{ref}/N_{ref}$, where E and E_{ref} are respectively the energies of nanosheets and corresponding bulk crystals. N and N_{ref} are the numbers of atoms in the respective unit cells. The calculated formation energies of monolayer α-M_2X_3, few-layer α-Ga_2S_3 and α-In_2Se_3 are shown in Fig. 2. The formation energies of α-M_2X_3 monolayers are comparable or even smaller than that of monolayer MoS_2. The formation energies of monolayer, bilayer

Table 1 Calculated in-plane constants a (Å), effective thicknesses h (Å), PBE bandgaps E_g^{PBE} (eV), HSE06 bandgaps E_g^{HSE06} (eV), minimum direct energy gaps E_{min}^{HSE06} (eV) and SHG coefficients $\chi^{(2)}(0)$ (pm V^{-1}) of monolayer α-M_2X_3 (M = Ga, In; X = S, Se), few-layer α-Ga_2S_3 and α-In_2Se_3

		a	h	E_g^{PBE}	E_g^{HSE06}	E_{min}^{HSE06}	$\chi^{(2)}_{xxy}(0)$	$\chi^{(2)}_{zxx}(0)$	$\chi^{(2)}_{zzz}(0)$
α-Ga_2S_3	ML	3.59	8.94	1.79(I)	2.95(I)	3.25(G)	25.4	23.8	162.6
	AA	3.59	17.88	0.65(I)	1.80(I)	2.05(G)	23.0	27.4	184.2
	AB	3.59	17.88	1.64(I)	2.80(I)	3.04(G)	25.0	−0.3	0.8
	ABA	3.59	26.82	1.52(I)	2.64(I)	2.81(G)	24.2	6.4	47.6
α-Ga_2Se_3	ML	3.77	9.40	1.06(I)	2.04(I)	2.30(G)	34.6	26.2	208.0
α-In_2S_3	ML	3.83	9.18	1.29(I)	2.30(I)	2.36(G)	30.6	36.6	207.6
α-In_2Se_3	ML	3.99	9.68	0.88(I)	1.80(I)	1.83(G)	42.2	41.8	252.6
	AB	3.99	19.36	0.57(I)	1.45(I)	1.46(G)	44.0	−1.80	−0.02
	ABA	4.00	29.04	0.45(I)	1.25(I)	1.26(G)	48.2	8.2	61.4

AA, and trilayer AAA α-Ga_2S_3 (α-In_2Se_3) decrease as their layer numbers increase, suggesting it is more likely to successfully obtain α-Ga_2S_3 (α-In_2Se_3) nanosheets with larger layer numbers. Indeed, trilayer AAA α-In_2Se_3, *i.e.* 3.1 nm-thick α-In_2Se_3 nanosheets have been synthesized using mechanical exfoliation.[23] Moreover, the formation energy of α-Ga_2S_3 nanosheets is to some extent smaller than that of corresponding α-In_2Se_3 nanosheets, indicating it is more likely to obtain α-Ga_2S_3 nanosheets. Furthermore, the difference of the formation energy can be negligible for AA (AAA) and AB (ABA), ensuring the feasibility to achieve AB (ABA) by switching the electric dipole orientation in AA (AAA) from the standpoint of energetics.

3.2. Electronic properties

In contrast to the previous bandgap calculation using the HSE06 functional with 25% exact exchange,[25] we calculated the band structure of single-layer α-M_2X_3 using 30% EE, *cf.* ESI (SI-1†). The calculated band structures are displayed in Fig. 3. α-M_2X_3 monolayers are indirect bandgap semiconductors with their valence band maximum (VBM) located between the M (0.0, 0.5, 0.0) and gamma (0.0, 0.0, 0.0) points. The conduction band minimum (CBM) is located at the M point for monolayer α-Ga_2S_3 and α-Ga_2Se_3, while for single-layer α-In_2S_3 and α-In_2Se_3 it is located at the gamma point. The top valence band of α-M_2X_3 monolayers is relatively flat, resulting in a high density of electronic states in the top valence band region as shown in Fig. 3(e), which is the origin of large SHG coefficients.[7]

Table 1 summarizes the PBE and HSE06 bandgaps of α-M_2X_3 monolayers. The PBE bandgap of 0.88 eV for monolayer α-In_2Se_3 gets very close to the calculated bandgap of 0.82 eV using PBE + SOC,[24] suggesting spin-orbital coupling (SOC) does not significantly modify the electronic property. The HSE06 bandgap of 1.80 eV for single-layer α-In_2Se_3 gets close to the calculated bandgap of 1.92 eV using the GW approximation,[24] but slightly larger than the bandgap of 1.45 eV calculated using HSE06 with 25% exact exchange.[25] The energy gaps of each monolayer at the gamma point are close to their respective indirect bandgaps, which is more evident for α-In_2S_3 and α-In_2Se_3 monolayers. It is expected the interband optical transition at the gamma point improves optical responses of α-M_2X_3 monolayers because no phonons are required for this optical transition to proceed. Additionally, the HSE06 bandgaps of α-M_2X_3 monolayers are large enough to avoid current leakages, and thereby they are promising in piezoelectric devices.

Fig. 4 displays the band structures of bilayer AA and AB, and trilayer ABA α-Ga_2S_3 calculated using HSE06. If there were no interlayer interaction, the band structure of bilayer AA α-Ga_2S_3 should be identical to that of monolayer α-Ga_2S_3. Nevertheless, the bands from different α-Ga_2S_3 layers in AA are pronouncedly splitted. Comparisons of Fig. 3(c) and 4(c) show the bottom valence bands from various α-Ga_2S_3 layers in AA are splitted by as large as 1.31 eV. Resultantly, the bandgap of AA significantly gets reduced by 1.15 eV in comparison with that of monolayer α-Ga_2S_3 as Table 1 shows, and that of trilayer AAA α-Ga_2S_3 further decreases as shown in Fig. 4(a). In brief, we find the bandgap of

Fig. 2 Calculated formation energies of monolayer α-M_2X_3, few-layer α-Ga_2S_3 and α-In_2Se_3. The formation energy of the synthesized MoS_2 monolayer is shown for comparison.

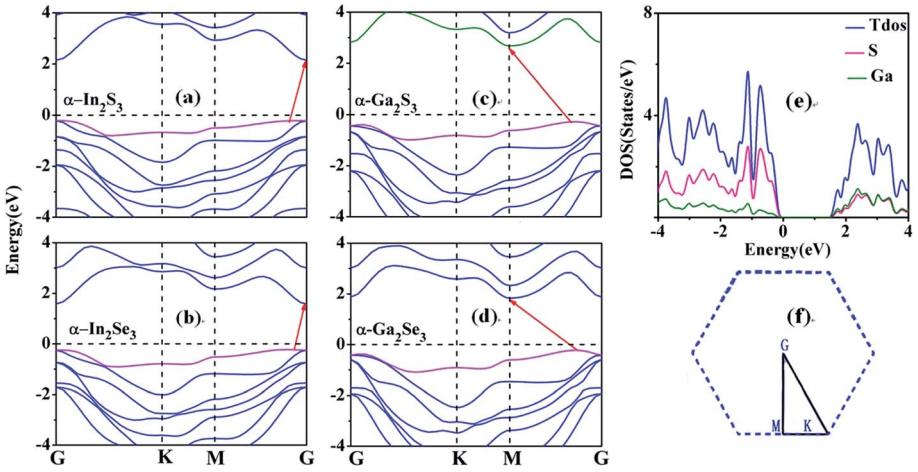

Fig. 3 Calculated band structure of (a) α-In_2S_3, (b) α-In_2Se_3, (c) α-Ga_2S_3 and (d) α-Ga_2Se_3 using HSE06 incorporating 30% EE. (e) Total and partial density of states of monolayer α-Ga_2S_3 calculated using PBE. (f) The high symmetry *k*-point path in the Brillouin Zone is chosen as: gamma (0, 0, 0) → *k* (−1/3, 2/3, 0) → *M* (0, 1/2, 0) → gamma (0, 0, 0), and gamma is abbreviated as G.

few-layer α-Ga_2S_3 nanosheets becomes much narrower as their layer number increases. This bandgap reduction is also pronounced for few-layer α-In_2Se_3 nanosheets. Fig. 4(a) indicates the bandgap of trilayer AAA α-In_2Se_3 nearly vanishes. Similarly, optical absorption spectra show the bandgap decreases from 2.80 eV to 1.45 eV as the layer thickness increases from 3.1 nm to 20.1 nm.[23] Considering the effective thickness of monolayer α-In_2Se_3 is ~1 nm, the optical bandgap of 1.45 eV for α-In_2Se_3 nanosheets with ~20 layers gets close to our theoretical value of 1.48 eV for α-In_2Se_3 bulk crystals. Nevertheless, the experimental bandgap of 2.8 eV for 3.1 nm-thick (trilayer) α-In_2Se_3 nanosheets significantly varies from the zero bandgap of trilayer AAA α-In_2Se_3. Moreover, PBE calculations also find the bandgap of bilayer AA and trilayer AAA α-In_2Se_3 is closed.[25] It seems further bandgap measurements of few-layer α-In_2Se_3 are emergently needed to interpret the huge divergence between experimental and theoretical bandgaps. On the other hand, we note the band splitting in non-ferroelectric MoS_2 nanosheets is not so pronounced.[35] Single-layer MoS_2 embodies out-of-plane centrosymmetric characters and in-plane non-centrosymmetric characters. Therefore, the pronounced band splitting in few-layer α-Ga_2S_3 (α-In_2Se_3) nanosheets is caused by the built-in electric field originated from the parallel out-of-plane electric polarizations (dipoles) of α-Ga_2S_3 (α-In_2Se_3) layers (*cf.* ESI-3†). This is further affirmed by semiconducting α-In_2Se_3 monolayers becoming metallic when an electric filed perpendicular is applied.[24]

The band splitting of bilayer AB α-Ga_2S_3 is not pronounced, and accordingly the bandgap difference between monolayer and bilayer AB α-Ga_2S_3 is very small. This is because the built-in electric field significantly decreases as the out-of-plane electric polarizations (dipoles) of α-Ga_2S_3 layers are antiparallelly

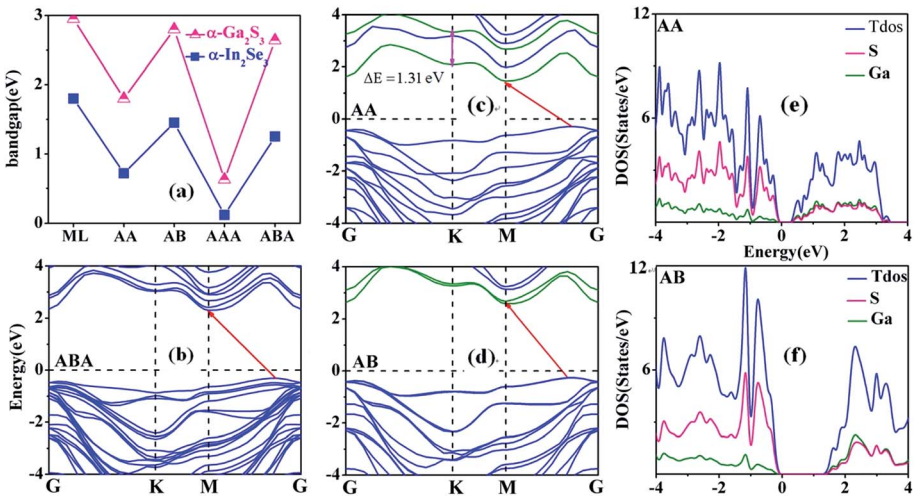

Fig. 4 (a) Bandgap variation of monolayer (ML), bilayer AA and AB, trilayer AAA and ABA α-Ga_2S_3 (α-In_2Se_3) nanosheets. Calculated Band structure of bilayer (c) AA and (d) AB, and (b) trilayer ABA α-Ga_2S_3 calculated using HSE06. Total and partial density of states (DOS) of bilayer (e) AA and (f) AB α-Ga_2S_3 calculated using PBE.

aligned (*cf.* ESI-3†). Furthermore, the band splitting in Fig. 4(b) is minor in ABA α-Ga_2S_3 as expected. The divergence of electronic properties between AA and AB α-Ga_2S_3 is further emphasized in Fig. 4(e) and (f). The peaks in the conduction band region of bilayer AB α-Ga_2S_3 look similar to that of monolayer α-Ga_2S_3. Nevertheless, the peaks in AA α-Ga_2S_3 are significantly splitted, particularly for the peaks between −3 and −2 eV. Briefly, the bandgap in AA α-Ga_2S_3 is broadened by 1.00 eV in AB α-Ga_2S_3, which is very advantageous for applications as photodetectors since one can select the sensing photon energy window by switching electric dipole orientation. Additionally, the zero bandgap in AAA α-In_2Se_3 is opened in ABA α-In_2Se_3, indicating the semiconducting nature can be achieved by switching the electric dipole orientation.

3.3. SHG properties

The length-gauge formulism at the independent-particle level derived by Aversa and Sipe[37] and rearranged by Rashkeev *et al.*[38] is used to calculate second-harmonic generation (SHG) coefficients (*cf.* ESI-2†), and its details are displayed in a previous work.[39] Similar to previous works,[7,27] the energy differences between HSE06 and PBE bandgaps are used for scissors corrections to reduce the errors caused by neglected many-body effects;[40–42] the effective unit cell volume is applied to reduce underestimations caused by the large vacuum spacing. For α-M_2X_3 monolayers and few-layers, the effective volume is obtained by multiplying the area of in-plane unit cell and the effective thickness.

Because single- and few-layer α-M_2X_3 belong to C_{3v} symmetry, they have eleven static SHG coefficients and only three of them are independent dictated by Kleiman's symmetry: $\chi^{(2)}_{yyy}(0) = -\chi^{(2)}_{yxx}(0) = -\chi^{(2)}_{xxy}(0) = -\chi^{(2)}_{xyx}(0)$, $\chi^{(2)}_{zzz}(0)$ and $\chi^{(2)}_{zxx}(0) = \chi^{(2)}_{zyy}(0) = \chi^{(2)}_{yyz}(0) = \chi^{(2)}_{yzy}(0) = \chi^{(2)}_{xzx}(0) = \chi^{(2)}_{xxz}(0)$. The static $\chi^{(2)}_{xxy}(0)$, $\chi^{(2)}_{zxx}(0)$ and $\chi^{(2)}_{zzz}(0)$ are summarized in Table 1. The static $\chi^{(2)}_{xxy}(0)$ describes the in-plane SHG phenomenon, which has been discovered in previous experiments of MoS_2,[2] GaSe[4] and BN[43] monolayers. Even though the static $\chi^{(2)}_{xxy}(0)$ of α-M_2X_3 monolayers is much smaller than that of MoS_2 (ref. 35) and GaSe[27] monolayers, it is still comparable with $\chi^{(2)}_{zxy}(0)$ of 28.2 pm V^{-1} for an archetypical nonlinear optical crystal $AgGaS_2$,[44] ensuring α-M_2X_3 monolayers can be used as in-plane two-dimensional SHG devices. More importantly, α-M_2X_3 monolayers have additional SHG components $\chi^{(2)}_{zzz}(0)$ and $\chi^{(2)}_{zxx}(0)$ compared with MoS_2 and GaSe monolayers. Especially, the calculated $\chi^{(2)}_{zzz}(0)$ of α-M_2X_3 monolayers are comparable or even larger than the static SHG coefficient of 173.2 pm V^{-1} for GaAs crystals.[45] Therefore, α-M_2X_3 monolayers are of great importance in ultrathin two-dimensional devices allowing strong out-of-plane SHG occurs.

Fig. 5 represents the calculated real and imaginary parts of SHG coefficients $\chi^{(2)}_{zzz}(-2\omega,\omega,\omega)$, $\chi^{(2)}_{zxx}(-2\omega,\omega,\omega)$ and $\chi^{(2)}_{xxy}(-2\omega,\omega,\omega)$ of α-M_2X_3 monolayers. The $\chi^{(2)}_{zzz}(-2\omega,\omega,\omega)$ and $\chi^{(2)}_{xxy}(-2\omega,\omega,\omega)$ components are significant in the entire range of optical energy. The $\chi^{(2)}_{zzz}(-2\omega,\omega,\omega)$ component is several times larger than $\chi^{(2)}_{xxy}(-2\omega,\omega,\omega)$ and $\chi^{(2)}_{zxx}(-2\omega,\omega,\omega)$. For $\chi^{(2)}_{zxx}(-2\omega,\omega,\omega)$, the electric field of both incoming and outgoing photons is parallel to the *z* axis, and thereby the electric depolarization vanishes. To analyze the prominent features in SHG spectra, the absolute values of imaginary part of $\chi^{(2)}_{zzz}(-2\omega,\omega,\omega)$ and $\chi^{(2)}_{xxy}(-2\omega,\omega,\omega)$ for monolayer α-Ga_2S_3 are plotted in Fig. 6 and compared with the absorptive part of corresponding dielectric function ε''. The first prominent peak between 1.7 and 3.8 eV in the $\chi^{(2)}_{zzz}(-2\omega,\omega,\omega)$ spectrum is caused by double-photon resonances (*cf.* Fig. 6(a) and (b)). In contrast, the double-peak structure between 3.8 and 5.6 eV in $\chi^{(2)}_{zzz}(-2\omega,\omega,\omega)$ comes from single- and double-photon resonances. These single- and double-photon resonances only involve optical transitions for the electric filed vector $\vec{E}$ parallel to the *z* axis ($\vec{E}\|z$). Fig. 6 further suggests the first prominent peak between 2.2 and 3.6 eV in the $\chi^{(2)}_{xxy}(-2\omega,\omega,\omega)$ spectrum is

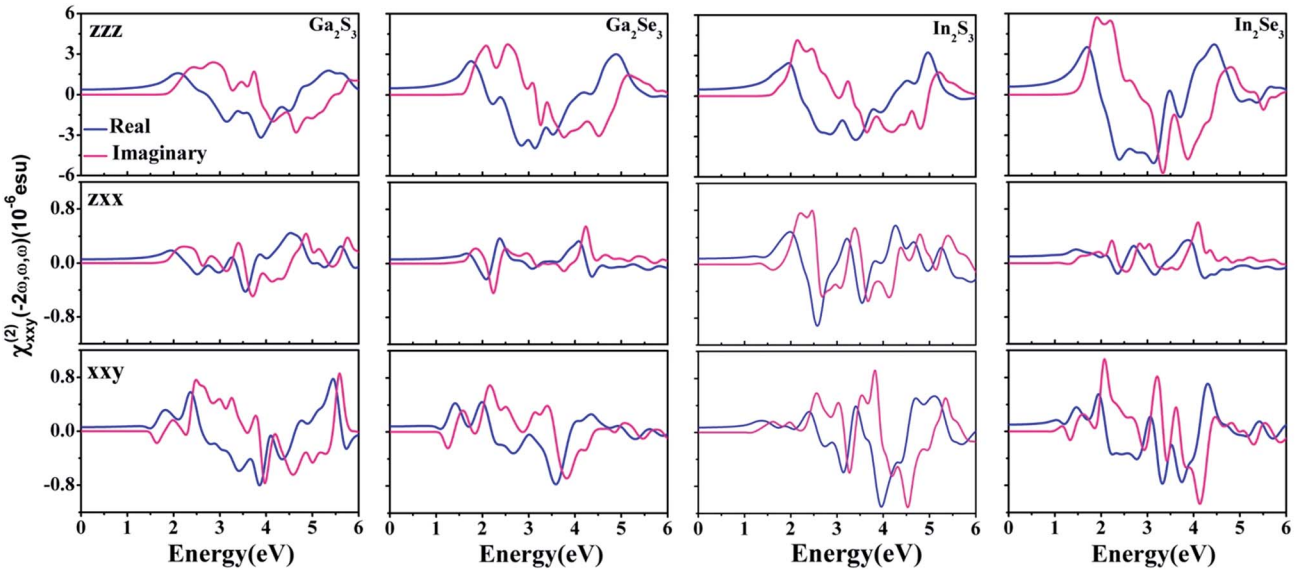

Fig. 5 Calculated real and imaginary parts of SHG coefficients $\chi^{(2)}_{zzz}(-2\omega,\omega,\omega)$, $\chi^{(2)}_{zxx}(-2\omega,\omega,\omega)$ and $\chi^{(2)}_{xxy}(-2\omega,\omega,\omega)$ of monolayer α-M_2X_3.

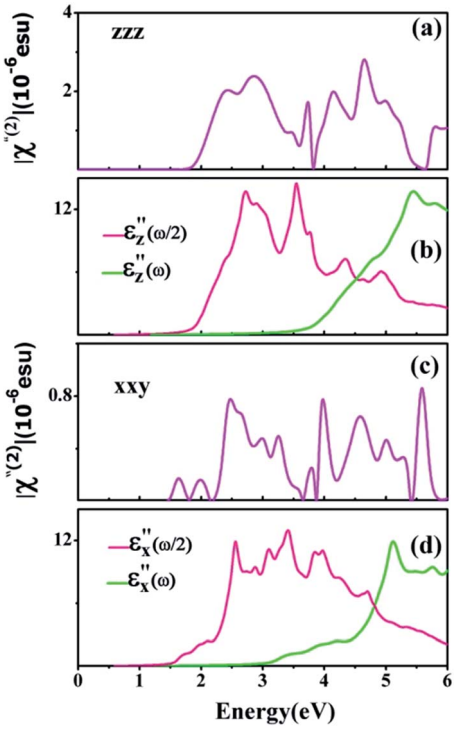

Fig. 6 (a) Absolute value of the imaginary part of $\chi^{(2)}_{zzz}(-2\omega,\omega,\omega)$, (b) imaginary part of the dielectric function ε''_z as a function of $\omega/2$ and ω, (c) absolute value of the imaginary part of $\chi^{(2)}_{xxy}(-2\omega,\omega,\omega)$, and (d) imaginary part of the dielectric function ε''_x as a function of $\omega/2$ and ω of monolayer α-Ga_2S_3.

caused by double-photon resonances with $\vec{E}\|x$ (*cf.* Fig. 6(c) and (d)), while the peak between 3.9 and 5.4 eV in $\chi^{(2)}_{xxy}(-2\omega,\omega,\omega)$ comes from both single- and double-photon resonances with $\vec{E}\|x$.

As shown in Table 1, the HSE06 bandgaps of few-layer α-Ga_2S_3 are in the visible range. In contrast, the HSE06 bandgaps of few-layer α-In_2Se_3 and AAA α-Ga_2S_3 are much narrower, which promises low laser damage thresholds. Therefore, we focus on SHG properties of bilayer AA and AB, and ABA α-Ga_2S_3, and their real and imaginary parts of $\chi^{(2)}_{zzz}(-2\omega,\omega,\omega)$, $\chi^{(2)}_{zxx}(-2\omega,\omega,\omega)$ and $\chi^{(2)}_{xxy}(-2\omega,\omega,\omega)$ are displayed in Fig. 7. The line shape of the three SHG spectra of AA α-Ga_2S_3 is very similar to that of monolayer α-Ga_2S_3, and the SHG spectra of AA are significantly redshifted in comparison with that of monolayer α-Ga_2S_3 because of the sizable bandgap reduction. Moreover, the calculated $\chi^{(2)}_{zzz}(0)$, $\chi^{(2)}_{zxx}(0)$ and $\chi^{(2)}_{xxy}(0)$ of AA α-Ga_2S_3 are very close to those of monolayer α-Ga_2S_3, respectively. These suggest that optical transitions occur within each α-Ga_2S_3 layer, namely the SHG property of each α-Ga_2S_3 layer is not modified by the built-in electric field of the neighboring α-Ga_2S_3 layer. According to the electric dipole theory, the SHG intensity shows a quadratic dependence on the SHG coefficient and the layer thickness,[4] and thereby the non-resonant SHG intensity in bilayer AA is about four times that in monolayers.

The redshift of $\chi^{(2)}_{xxy}(-2\omega,\omega,\omega)$ for AB α-Ga_2S_3 is negligible as the bandgap difference of monolayers and AB is small. $\chi^{(2)}_{zzz}(-2\omega,\omega,\omega)$ and $\chi^{(2)}_{zxx}(-2\omega,\omega,\omega)$ of AB α-Ga_2S_3 nearly vanishes, which is further corroborated by its vanishing static $\chi^{(2)}_{zzz}(0)$ and $\chi^{(2)}_{zxx}(0)$. The electric dipole in the $z(x)$ direction of the top and bottom α-Ga_2S_3 layers in bilayer AB points oppositely, and accordingly their contribution to the static $\chi^{(2)}_{zzz}(0)(\chi^{(2)}_{zxx}(0))$ cancels each other. The electric dipole in the z direction is the out-of-plane electric dipole, while the electric dipole in the x direction is the in-plane electric dipole. The $\chi^{(2)}_{zzz}(-2\omega,\omega,\omega)$ component of trilayer ABA α-Ga_2S_3 is 1/3 that of monolayer α-Ga_2S_3 as the contribution of the middle and bottom layers to $\chi^{(2)}_{zzz}(-2\omega,\omega,\omega)$ in trilayer ABA cancels each other. Therefore, we propose that one can effectively tune the out-of-plane SHG coefficient by switching the electric dipole orientation in 2D nanosheets. Additionally, we summarize $\chi^{(2)}(0)$ of AB and ABA α-In_2Se_3 in Table 1, which indicates the obtained optical rules are valid for other α-M_2X_3 nanosheets. The SHG property of few-layer α-In_2Se_3 in recent experiments could be obtained by analogy.[16]

3.4. Piezoelectric properties

To obtain piezoelectric strain coefficients d_{ij} which measure mechanical–electrical energy conversion ratios, we calculate elastic constants C_{ij} and piezoelectric stress coefficients e_{ij} using density functional perturbation theory (DFPT).[46] The clamped-ion elastic and piezoelectric coefficients are obtained from purely electronic contributions, while the relaxed-ion coefficients are obtained from the sum of electronic and ionic contributions. The relaxed-ion elastic and piezoelectric coefficients are physically meaningful and can be directly compared with experimental results. As shown in Table 2, single- and few-layer α-M_2X_3 have three independent elastic constants: C_{11}, C_{12} and C_{66}. The calculated clamped-ion and relaxed-ion elastic constants follow the correlation of $C_{66} \approx (C_{11} - C_{12})/2$. The relaxed-ion elastic constants fulfil the Born criteria of stability of 2D hexagonal structures,[47–49] *i.e.* $C_{11} > 0$ and C_{11}–$C_{12} > 0$, ensuing these monolayers and few-layers are mechanically stable. The calculated relaxed-ion Young's moduli ($Y = (C_{11}^2 - C_{12}^2)/C_{11}$) of single-layer α-M_2X_3 are smaller than that of graphene (341 N m^{-1}) and monolayer BN (275.9 N m^{-1}),[50] and comparable with that of monolayer TMDCs.[51] Therefore, α-M_2X_3 monolayers are much softer than graphene and monolayer BN, and their stiffness is comparable with that of monolayer TMDCs. Moreover, the calculated Young's moduli of bilayer (trilayer) α-Ga_2S_3 are about two (three) times that of monolayer α-Ga_2S_3. This is because, of the same strain, the force needed for bilayers (trilayers) is two (three) times that of monolayers.

Single- and few-layer α-M_2X_3 have two independent piezoelectric stress coefficients e_{11} and e_{31} dictated by C_{3v} symmetry. The piezoelectric strain coefficients d_{11} and d_{31}, which respectively measure the mechanical–electrical energy conversion ratios in x and z directions, are expressed as $d_{11} = e_{11}/(C_{11} - C_{12})$ and $d_{31} = e_{31}/(C_{11} + C_{12})$.[12] The relaxed-ion e_{11} values of monolayer α-Ga_2S_3 and α-Ga_2Se_3 in Fig. 8(a) are even larger than that of monolayer 2H-$CrTe_2$, which has the largest e_{11} of 654 pC m^{-1} among TMDCs.[12] The relaxed-ion d_{11} values of single-layer α-Ga_2Se_3 and α-In_2Se_3 in Fig. 8(c) are comparable with the maximum d_{11} of 13.45 pm V^{-1} for monolayer TMDCs, and

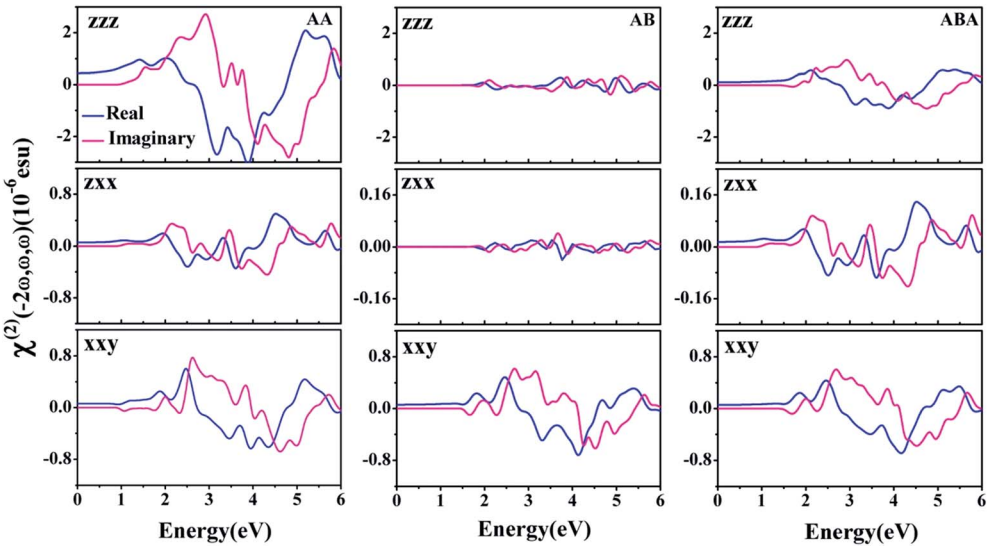

Fig. 7 Calculated real and imaginary parts of SHG coefficients $\chi^{(2)}_{zzz}(-2\omega,\omega,\omega)$, $\chi^{(2)}_{zxx}(-2\omega,\omega,\omega)$ and $\chi^{(2)}_{xxy}(-2\omega,\omega,\omega)$ of bilayer AA, AB, and trilayer ABA α-Ga_2S_3.

larger than the maximum d_{11} of 8.47 pm V^{-1} for Janus group-III chalcogenide monolayers.[11] The relaxed-ion d_{11} values of α-In_2S_3 and α-In_2S_3 monolayers are comparable with the maximum d_{11} of 2.30 pm V^{-1} for group-III chalcogenides.[10] Therefore, α-M_2X_3 monolayers are promising in ultrathin piezoelectric sensors and nano-generators. Fig. 8(a) and (c) further suggest the electronic and ionic polarizations of α-Ga_2S_3 and α-Ga_2Se_3 monolayers both positively contribute to relaxed-ion piezoelectric coefficients e_{11} and d_{11}, resulting in significant in-plane piezoelectricity. In contrast, the electronic and ionic polarizations of α-In_2S_3 and α-In_2Se_3 monolayers oppositely contribute to relaxed-ion e_{11} and d_{11}, resulting in smaller in-plane piezoelectricity. Our calculation also generates relaxed-ion e_{11} and d_{11} are respectively 369 pC m^{-1} and 3.72 pm V^{-1} for monolayer MoS_2, in good agreement with previous theoretical values of 364 pC m^{-1} and 3.73 pm V^{-1},[8] indicating our theoretical results are numerically reliable.

Fig. 8(b) and (d) suggest α-M_2X_3 monolayers have nonzero out-of-plane piezoelectric coefficients e_{31} and d_{31}. The electronic and ionic polarizations of all α-M_2X_3 monolayers both negatively contribute to e_{31} and d_{31}. The d_{31} values of α-M_2X_3 monolayers are comparable with the maximum d_{31} of 0.46 pm V^{-1} for monolayer Janus group-III chalcogenides[11] and the maximum d_{31} of 0.658 pm V^{-1} for bucked hexagonal compounds.[12] However, the bucked hexagonal compounds are energetically metastable. In contrast, α-M_2X_3 monolayers are energetically, dynamically[25] and mechanically stable, ensuing they are experimentally feasible.

The calculated piezoelectric coefficients e_{11} and e_{31} of AA and AB α-Ga_2S_3 are summarized in Fig. 8(e), while their d_{11} and d_{31} coefficients are displayed in Fig. 8(f). Comparisons of Fig. 8(a) and (e) show the clamped-ion (relaxed-ion) e_{11} of AB α-Ga_2S_3 is exactly twice that of monolayer α-Ga_2S_3. This is because, of the same strain, the change of polarization charges in the x direction of bilayer AB α-Ga_2S_3 is twice that of monolayer α-Ga_2S_3. Therefore, the piezoelectric effect occurs within each α-Ga_2S_3 layer in AB, namely the piezoelectricity of each α-Ga_2S_3 layer is not modified by the built-in electric field of the neighboring α-Ga_2S_3 layer. This is further affirmed by the relaxed-ion d_{11} of 10.4 pm V^{-1} for AB α-Ga_2S_3 being very close to that (10.7 pm V^{-1}) for monolayer α-Ga_2S_3. The relaxed-ion d_{31} of bilayer AB nearly vanishes since the piezoelectric contribution to d_{31} of each α-Ga_2S_3 layer cancels each other.

Fig. 8(a) and (e) further suggest the clamped-ion e_{11} of 485.1 pC m^{-1} for bilayer AA α-Ga_2S_3 is exactly twice that (243.6 pC m^{-1}) of monolayer α-Ga_2S_3, while the relaxed-ion e_{11} of 1350.3 pC m^{-1} for AA α-Ga_2S_3 is to some extent smaller than twice that (755.6 pC m^{-1}) of monolayer α-Ga_2S_3. The clamped-ion e_{31} of −240.2 pC m^{-1} for AA α-Ga_2S_3 is much larger than that (−11.4 pC m^{-1}) of monolayer α-Ga_2S_3, namely the clamped-ion e_{31} of AA α-Ga_2S_3 is much enhanced by the strong built-in electric field originated from the parallel out-of-plane electric polarizations of α-Ga_2S_3 layers. The relaxed-ion d_{31} of −0.91 pm V^{-1} for AA α-Ga_2S_3 is accordingly several times larger

Table 2 Theoretical elastic constants C_{ij} and Yang moduli Y (N m^{-1}) in both clamped- and relaxed-ion cases of monolayer α-M_2X_3 and few-layer α-Ga_2S_3

		Clamped-ion				Relaxed-ion			
		C_{11}	C_{12}	C_{66}	Y	C_{11}	C_{12}	C_{66}	Y
α-Ga_2S_3	ML	146.7	48.6	48.9	130.5	115.5	45.0	35.1	104.3
	AA	293.3	97.6	97.6	261.0	228.2	83.3	72.4	197.7
	AB	292.3	96.2	97.6	260.6	224.3	85.4	69.3	191.7
	ABA	439.2	145.8	146.7	390.7	348.7	134.5	106.6	296.8
	AB ab								
α-Ga_2Se_3	ML	120.9	39.9	40.2	107.7	91.8	42.0	24.6	72.5
α-In_2S_3	ML	117.0	43.2	36.6	101.0	75.6	36.6	19.2	57.8
α-In_2Se_3	ML	96.3	35.1	30.6	83.5	68.4	24.0	21.9	59.9

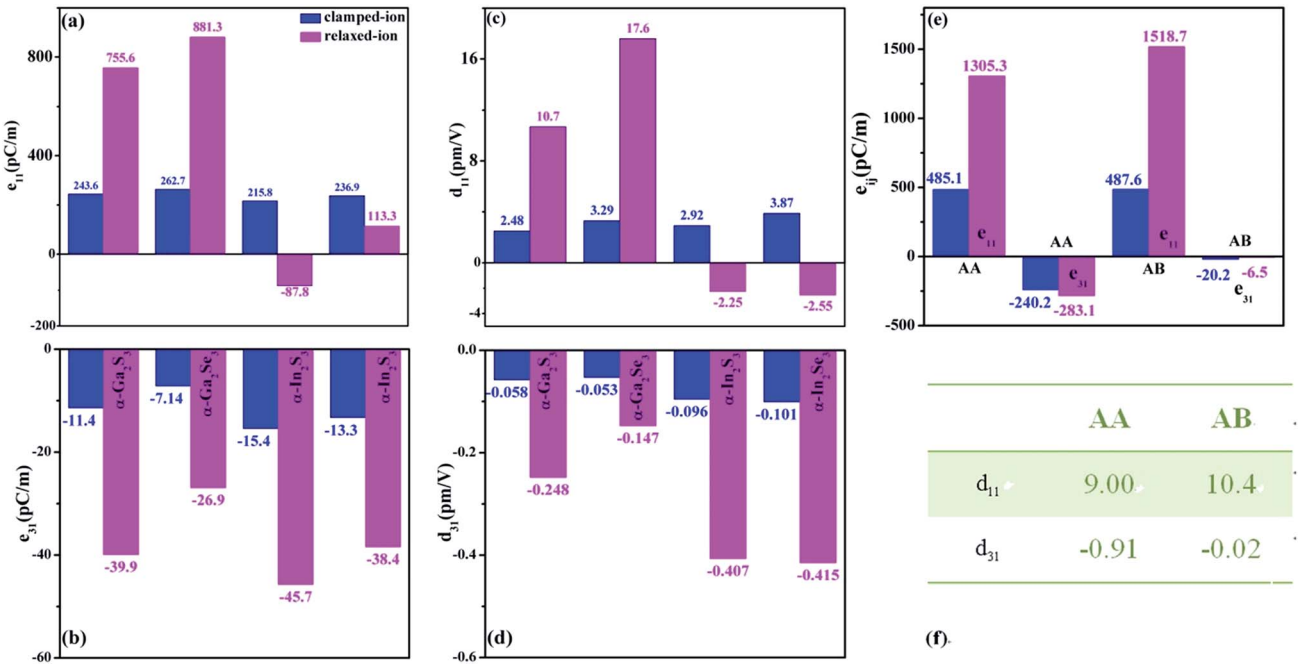

Fig. 8 Piezoelectric coefficients (a) e_{11}, (b) e_{31}, (c) d_{11} and (d) d_{31} of monolayer α-M_2X_3 in clamped- and relaxed-ion cases. (e) Clamped- and relaxed-ion e_{11} and e_{31} of bilayer AA and AB α-Ga_2S_3. (f) Relaxed-ion d_{11} and d_{31} (pm V^{-1}) of AA and AB α-Ga_2S_3.

than that (−0.248 pm V^{-1}) of monolayer α-Ga_2S_3, suggesting AA α-Ga_2S_3 is much more easily polarized than monolayer α-Ga_2S_3. Similarly, the electric dipole (0.165 eÅ) of AA α-In_2Se_3 is much larger than that (0.07 eÅ) of monolayer α-In_2Se_3.[25]

Briefly, we find AA α-Ga_2S_3 has the largest out-of-plane d_{31} among all atomic-thick 2D materials up to date. More importantly, the built-in electric field can induce strong out-of-plane piezoelectricity in atomic-thick 2D materials, which is corroborated by a recent calculation which finds large d_{31} of −1.234 pm V^{-1} and d_{33} of −13.517 pm V^{-1} in multilayer MoSTe.[15] However, the large $d_{33}(\partial P_3/\partial\sigma_3$, P is the electric polarization and σ is the stress) in multilayer MoSTe will vanish in atomic-thick 2D MoSTe such as monolayer[15] and bilayer MoSTe (*cf.* ESI-4†). This reflects it is very difficult to impose stresses along the z direction for atomic-thick 2D materials since their effective thickness is far smaller than their flake size. For instance, the effective thickness of monolayer MoSSe is about 6.3 Å while its flake size is more than 5 μm.[52] The effective thickness of monolayer MoSSe is considered as the average of that of MoS_2 and $MoSe_2$ monolayers.[35] In contrast, it is easy to impose stresses along the x direction to achieve large $d_{31}(\partial P_3/\partial\sigma_1)$ because of the large size of atomic-thick 2D materials. Therefore, it is more reasonable to induce out-of-plane piezoelectricity by imposing stresses along the x direction within atomic-thick 2D materials. Moreover, the d_{31} coefficient of −1.234 pm V^{-1} for multilayer MoSTe decreases to −0.417 pm V^{-1} of bilayer MoSTe (*cf.* ESI-4†), being smaller than that of AA Ga_2S_3. The small bandgap of AAA α-Ga_2S_3 is disadvantageous to avoid current leakages. The piezoelectric coefficient d_{11} of ABA α-Ga_2S_3 should be close to that of monolayer α-Ga_2S_3, while its d_{31} coefficient is around 1/3 that of monolayer α-Ga_2S_3 since the piezoelectric response occurs within each α-Ga_2S_3 layer.

4. Summaries

We have carried out first-principles calculations of structural, electronic, SHG and piezoelectric properties of single- and few-layer α-M_2X_3 (M = Ga, In; X = S, Se). Firstly, α-M_2X_3 few-layers are energetically favorable and mechanically stable, ensuring bilayer AA and trilayer AAA can be successfully attained by mechanical exfoliation and bilayer AB and trilayer ABA can be achieved by switching the electric dipole orientation. Secondly, the relative flat top valence band of α-M_2X_3 monolayer promises large SHG coefficients, and their large bandgaps are helpful to avoid current leakages in piezoelectric devices. The splitting of energy bands in few-layer AA and AAA is very pronounced because of the built-in electric field originated from the parallel out-of-plane electric dipoles, while in contrast, that of AB and ABA is not pronounced because the built-in electric field significantly diminishes as the out-of-plane electric dipoles are antiparallelly aligned. Therefore, we propose a completely new method, *i.e.* switching the electric dipole orientation to tune electronic structures and bandgaps, which is very advantageous to tune the sensing photon energy window and achieve the semiconducting nature. Thirdly, the in-plane SHG coefficients of α-M_2X_3 monolayers are comparable with that of $AgGaS_2$ crystals. More importantly, we find out-of-plane SHG in α-M_2X_3 monolayers and their out-of-plane SHG coefficients are comparable with that of GaAs crystals. Furthermore, SHG occurs within each α-M_2X_3 layers in AA and AB, and accordingly one can achieve an enhanced out-of-plane SHG intensity in AA

and eliminate the out-of-plane SHG in AB. Fourthly, the stiffness of α-M_2X_3 monolayers is comparable that with monolayer TMDCs. α-M_2X_3 monolayers exhibit strong in-plane and considerable out-of-plane piezoelectricity. Furthermore, out-of-plane piezoelectricity vanishes in AB α-Ga_2S_3, and it is greatly enhanced in AA α-Ga_2S_3 as the electric dipoles are parallelly aligned. To our knowledge, out-of-plane SHG in 2D materials has been rarely reported, while the out-of-plane piezoelectricity is very limited in ultrathin 2D materials. Here we have presented strong out-of-plane SHG and piezoelectricity in ultrathin 2D materials. In general, our research will stimulate researches on the ultrathin 2D photo detection, SHG and piezoelectric devices.

Conflicts of interest

There are no conflicts to declare.

Acknowledgements

This work is supported by National Nature Science foundation of China (21373099, 21573090), Jilin Province Science and Technology Development Plan (20150101005JC) and the Ministry of Education of China (20130061110020). We also thank professor Yong-Fan Zhang in Fuzhou University for SHG calculation program developing.

References

1 D. Neshev and Y. Kivshar, *Science*, 2014, **344**, 483.
2 X. Yin, Z. Ye, D. A. Chenet, Y. Ye, K. O'Brien, J. C. Hone and X. Zhang, *Science*, 2014, **344**, 488.
3 W. Jie, X. Chen, D. Li, L. Xie, Y. Y. Hui, S. P. Lau, X. Cui and J. Hao, *Angew. Chem., Int. Ed.*, 2015, **54**, 1185.
4 X. Zhou, J. Cheng, Y. Zhou, T. Cao, H. Hong, Z. Liao, S. Wu, H. Peng, K. Liu and D. P. Yu, *J. Am. Chem. Soc.*, 2015, **137**, 7994.
5 I. J. Wu and G. Y. Guo, *Phys. Rev. B: Condens. Matter Mater. Phys.*, 2008, **78**, 035447.
6 G. Y. Guo and J. C. Lin, *Phys. Rev. B: Condens. Matter Mater. Phys.*, 2005, **72**, 075416.
7 L. Hu and D. S. Wei, *Phys. Chem. Chem. Phys.*, 2017, **19**, 2235.
8 K. A. N. Duerloo, M. T. Ong and E. J. Reed, *J. Phys. Chem. Lett.*, 2012, **3**, 2871.
9 H. Zhu, Y. Wang, J. Xiao, M. Liu, S. Xiong, Z. J. Wong, Z. Ye, Y. Ye, X. Yin and X. Zhang, *Nat. Nanotechnol.*, 2015, **10**, 151.
10 W. Li and J. Li, *Nano Res.*, 2015, **8**, 3796.
11 Y. Guo, S. Zhou, Y. Bai and J. Zhao, *Appl. Phys. Lett.*, 2017, **110**, 163102.
12 M. N. Blonsky, H. L. Zhuang, A. K. Singh and R. G. Hennig, *ACS Nano*, 2015, **9**, 9885.
13 M. T. Ong and E. J. Reed, *ACS Nano*, 2012, **6**, 1387.
14 W. Wu, L. Wang, Y. Li, F. Zhang, L. Lin, S. Niu, D. Chenet, X. Zhang, Y. Hao, T. F. Heinz, J. Hone and Z. L. Wang, *Nature*, 2014, **514**, 470.
15 L. Dong, J. Lou and V. B. Shenoy, *ACS Nano*, 2017, **11**, 8242.
16 Y. Zhou, D. Wu, Y. Zhu, Y. Cho, Q. He, X. Yang, K. Herrera, Z. Chu, Y. Han, M. C. Downer, H. Peng and K. Lai, *Nano Lett.*, 2017, **17**, 5508.
17 S. Zhou, X. Tao and Y. Gu, *J. Phys. Chem. C*, 2016, **120**, 4753.
18 X. Tao and Y. Gu, *Nano Lett.*, 2013, **13**, 3501.
19 G. Almeida, S. Dogan, G. Bertoni, C. Giannini, R. Gaspari, S. Perissinotto, R. Krahne, S. Ghosh and L. Manna, *J. Am. Chem. Soc.*, 2017, **139**, 3005.
20 R. B. Jacobs-Gedrim, M. Shanmugam, N. Jain, C. A. Durcan, M. T. Murphy, T. M. Murray, R. J. Matyi, R. L. Moore and B. Yu, *ACS Nano*, 2014, **8**, 514.
21 W. Feng, W. Zheng, F. Gao, X. Chen, G. Liu, T. Hasan, W. Cao and P. Hu, *Chem. Mater.*, 2016, **28**, 4278.
22 D. Wu, A. J. Pak, Y. Liu, Y. Zhou, X. Wu, Y. Zhu, M. Lin, Y. Han, Y. Ren, H. Peng, Y. Tsai, G. S. Hwang and K. Lai, *Nano Lett.*, 2015, **15**, 8136.
23 J. Quereda, R. Biele, G. Rubio-Bollinger, N. Agraït, R. D'Agosta and A. Castellanos-Gomez, *Adv. Opt. Mater.*, 2016, **4**, 1939.
24 L. Debbichi, O. Eriksson and S. Lebègue, *J. Phys. Chem. Lett.*, 2015, **6**, 3098.
25 W. Ding, J. Zhu, Z. Wang, Y. Gao, D. Xiao, Y. Gu, Z. Zhang and W. Zhu, *Nat. Commun.*, 2017, **8**, 14956.
26 H. Wang and X. Qian, *Nano Lett.*, 2017, **17**, 5027.
27 L. Hu, X. R. Huang and D. S. Wei, *Phys. Chem. Chem. Phys.*, 2017, **19**, 11131.
28 P. E. Blöchl, *Phys. Rev. B: Condens. Matter Mater. Phys.*, 1994, **50**, 17953.
29 G. Kresse and J. Furthmüller, *Phys. Rev. B: Condens. Matter Mater. Phys.*, 1996, **54**, 11169.
30 G. Kresse and J. Furthmüller, *Comput. Mater. Sci.*, 1996, **6**, 15.
31 G. Kresse and J. Hafner, *Phys. Rev. B: Condens. Matter Mater. Phys.*, 1993, **47**, 558.
32 G. Kresse and J. Hafner, *Phys. Rev. B: Condens. Matter Mater. Phys.*, 1994, **49**, 14251.
33 J. P. Perdew, K. Burke and M. Ernzerhof, *Phys. Rev. Lett.*, 1996, **77**, 3865.
34 S. Grimme, *J. Comput. Chem.*, 2006, **27**, 1787.
35 C. Y. Wang and G. Y. Guo, *J. Phys. Chem. C*, 2015, **119**, 13268.
36 H. L. Zhuang and R. G. Hennig, *Chem. Mater.*, 2013, **25**, 3232.
37 C. Aversa and J. E. Sipe, *Phys. Rev. B: Condens. Matter Mater. Phys.*, 1995, **52**, 14636.
38 S. N. Rashkeev, W. R. L. Lambrecht and B. Segall, *Phys. Rev. B: Condens. Matter Mater. Phys.*, 1998, **57**, 3905.
39 Z. Fang, J. Lin, R. Liu, P. Liu, Y. Li, X. Huang, K. Ding, L. Ning and Y. Zhang, *CrystEngComm*, 2014, **16**, 10569.
40 M. Grüning and C. Attaccalite, *Phys. Rev. B: Condens. Matter Mater. Phys.*, 2014, **89**, 081102.
41 H. C. Hsueh, G. Y. Guo and S. G. Louie, *Phys. Rev. B: Condens. Matter Mater. Phys.*, 2011, **84**, 085404.
42 F. Karlický and M. Otyepka, *Ann. Phys.*, 2014, **526**, 408.
43 Y. Li, Y. Rao, K. F. Mak, Y. You, S. Wang, C. R. Dean and T. F. Heinz, *Nano Lett.*, 2013, **13**, 3329.
44 L. Bai, Z. Lin, Z. Wang, C. Chen and M. H. Lee, *J. Chem. Phys.*, 2004, **120**, 8772.
45 Z. Ma, K. Wu, R. Sa, Q. Li and Y. Zhang, *J. Alloys Compd.*, 2013, **568**, 16.

46 X. Wu, D. Vanderbilt and D. R. Hamann, *Phys. Rev. B: Condens. Matter Mater. Phys.*, 2005, **72**, 035105.
47 H. L. Zhuang, M. D. Johannes, M. N. Blonsky and R. G. Hennig, *Appl. Phys. Lett.*, 2014, **104**, 022116.
48 M. Born and H. Huang, *Dynamical Theory of Crystal Lattices*, Clarendon Press, Oxford, 1954.
49 F. Mouhat and F. X. Coudert, *Phys. Rev. B: Condens. Matter Mater. Phys.*, 2014, **90**, 224104.
50 D. Çakır, F. M. Peeters and C. Sevik, *Appl. Phys. Lett.*, 2014, **104**, 203110.
51 M. M. Alyörük, Y. Aierken, D. Çakır, F. M. Peeters and C. Sevik, *J. Phys. Chem. C*, 2015, **119**, 23231.
52 J. Zhang, S. Jia, I. Kholmanov, L. Dong, D. Er, W. Chen, H. Guo, Z. Jin, V. B. Shenoy, L. Shi and J. Lou, *ACS Nano*, 2017, **11**, 8192.